Observations of Ekman Currents in the Southern Ocean

YUENG-DJERN LENN

School of Ocean Sciences, Bangor University, Menai Bridge, Wales, United Kingdom

TERESA K. CHERESKIN

Scripps Institution of Oceanography, University of California, San Diego, La Jolla, California

ABSTRACT

Largely zonal winds in the Southern Ocean drive an equatorward Ekman transport that constitutes the shallowest limb of the meridional overturning circulation of the Antarctic Circumpolar Current (ACC). Despite its importance, there have been no direct observations of the open ocean Ekman balance in the Southern Ocean until now. Using high-resolution repeat observations of upper-ocean velocity in Drake Passage, a mean Ekman spiral is resolved and Ekman transport is computed. The mean Ekman currents decay in amplitude and rotate anticyclonically with depth, penetrating to ~100-m depth, above the base of the annual mean mixed layer at 120 m. The rotation depth scale exceeds the *e*-folding scale of the speed by about a factor of 3, resulting in a current spiral that is compressed relative to predictions from Ekman theory. Transport estimated from the observed currents is mostly equatorward and in good agreement with the Ekman transport computed from four different gridded wind products. The mean temperature of the Ekman layer is not distinguishable from temperature at the surface. Turbulent eddy viscosities inferred from Ekman theory and a direct estimate of the time-averaged stress were $O(10^2-10^3)$ cm^2 s^{-1}. The latter calculation results in a profile of eddy viscosity that decreases in magnitude with depth and a time-averaged stress that is not parallel to the time-averaged vertical shear. The compression of the Ekman spiral and the nonparallel shear–stress relation are likely due to time averaging over the cycling of the stratification in response to diurnal buoyancy fluxes, although the action of surface waves and the oceanic response to high-frequency wind variability may also contribute.

1. Introduction

Circumpolar integration of the Southern Ocean Ekman transport results in estimates ranging from 25 to 30 Sv (1 Sv $\equiv 10^6$ m^3 s^{-1}; Sloyan and Rintoul 2001; Speer et al. 2000). The Ekman layer thus constitutes the shallowest limb of the meridional overturning circulation of the Antarctic Circumpolar Current (ACC), a key component of the coupled ocean–atmosphere climate system (Deacon 1937; Sloyan and Rintoul 2001; Speer et al. 2000). Despite the large transport, Ekman currents are difficult to observe because these currents are very small, typically only a few centimeters per second, and are masked by the larger pressure-driven flows, such as tides,

internal waves, and the geostrophic currents of the ACC. Highly variable Southern Ocean winds further complicate the extraction of mean Ekman currents from direct observations of upper-ocean velocities on any single cruise. The threat of mooring blowover and/or damage by icebergs prohibits moored observations of mixed-layer currents in the Southern Ocean. Therefore, despite their importance for global climate, Southern Ocean Ekman currents and transport have yet to be observed directly in the open ocean and are usually inferred from the wind using classical Ekman (1905) theory. Without direct measurement of the vertical profile of mean Ekman currents, accurate predictions of the Ekman layer depth, mean temperature, eddy viscosity, and associated Ekman layer heat fluxes cannot be made.

High-resolution, repeat shipboard observations of upper-ocean velocities and temperature in Drake Passage (Fig. 1) provide an opportunity to resolve the vertical profile of Southern Ocean Ekman currents and

Corresponding author address: Yueng-Djern Lenn, School of Ocean Sciences, Bangor University, Menai Bridge, Anglesey LL59 5AB, United Kingdom.
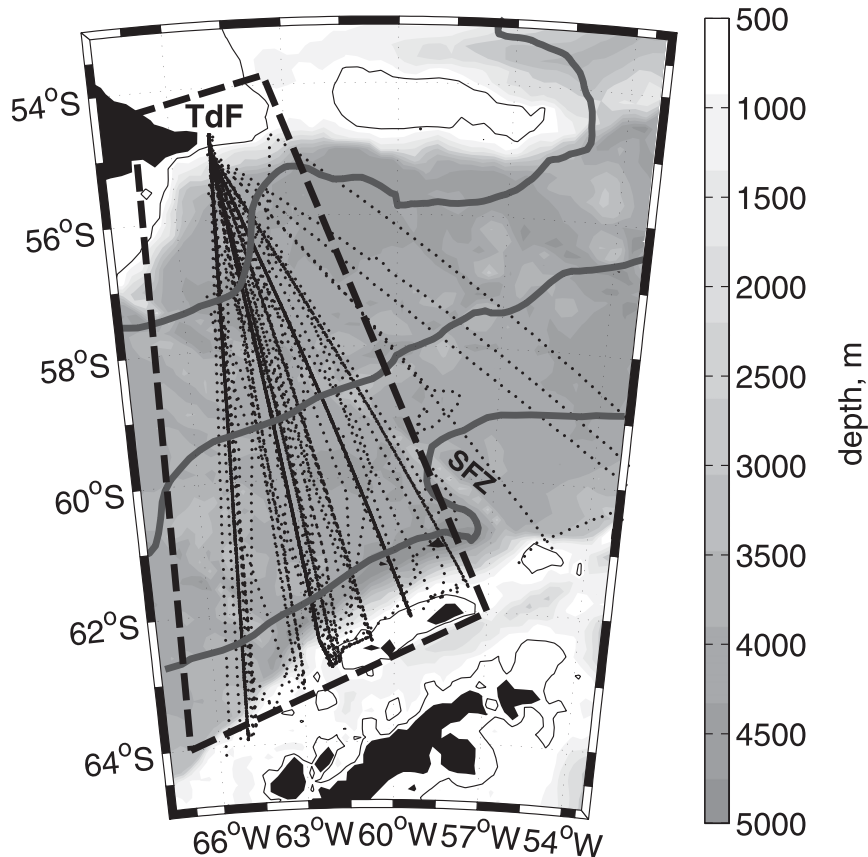E-mail: y.lenn@bangor.ac.uk

FIG. 1. Map of Drake Passage. Bathymetry is shaded in grayscale with *LMG* cruise tracks overlaid (dotted lines). Mean Ekman currents and wind stresses are computed from observations within the region bounded by the thick dashed line. Mean locations of the three main fronts of the ACC (from north to south: sub-Antarctic front, polar front, and southern ACC front) as determined by Orsi et al. (1995) are shown (thick gray lines). The geographic locations of Tierra del Fuego (TdF) and the Shackleton Fracture Zone (SFZ) are marked.

the mean Ekman layer transport. A summary of classical Ekman (1905) theory is provided in section 2. The Drake Passage datasets used in this analysis are described in section 3. The observed mean Ekman currents are presented in section 4. The balance between the mean wind stress and Ekman transport is discussed in section 5. The temperature of the Ekman layer is deduced in section 6, and a turbulent eddy viscosity is inferred in section 7. Our results and our conclusions are summarized in section 8.

2. Background

At high latitudes in the Southern Hemisphere, the largely zonal winds are expected to drive a time-averaged equatorward Ekman transport,

$$M_E \approx M_y = \int_{-h_E}^{0} \bar{v}_E \, dz = -\frac{1}{\rho f} \bar{\tau}_o^{\,x}, \tag{1}$$

where M_E is the Ekman transport, and M_y is its meridional component; h_E is the depth of the Ekman layer; v_E is the meridional Ekman current; ρ is the density of seawater; f is the Coriolis parameter; τ_o^x is the zonal component of the surface wind stress; and the overbar ($^-$) denotes time averaging. Ekman (1905) assumed that momentum from the wind is transferred downward by a turbulent stress $\tau(z)$ that is dependent on a constant eddy viscosity K and the vertical shear of the currents,

$$\text{if } \mathbf{U}_E = \frac{1}{\rho}\frac{\partial \boldsymbol{\tau}(z)}{\partial z} = K\frac{\partial^2 \mathbf{U}_E}{\partial z^2}, \tag{2}$$

where $\mathbf{U}_E = u_E + iv_E$ is the complex Ekman velocity and $\boldsymbol{\tau} = \tau^x + i\tau^y$ is the complex turbulent stress. Ekman's (1905) solutions for the steady winds acting on an infinitely deep homogeneous ocean describe currents that decay with depth and spiral anticyclonically from the surface ($z = 0$, z is positive upward). Their generalized form given as in Chereskin and Price (2001) is

$$\bar{u}_E = \exp(z/D_E)[V^+ \cos(z/D_E) + V^- \sin(z/D_E)], \quad \text{and}$$
(3)

$$\bar{v}_E = \exp(z/D_E)[V^+ \sin(z/D_E) - V^- \cos(z/D_E)], \quad (4)$$

where $V^{\pm} = (\tau_o^x \pm \tau_o^y)/(\rho\sqrt{2K|f|})$ depends on the surface wind stress $\boldsymbol{\tau}_o$ and the eddy viscosity K. The eddy viscosity also controls the vertical decay scale $D_E\sqrt{2K/|f|}$, over which the current amplitude decays by a factor of $1/e$ and the velocity vector rotates by 1 rad.

3. The Drake Passage datasets

a. ADCP observations

The underway shipboard acoustic Doppler current profiler (ADCP) data were collected by the Antarctic Research and Supply Vessel (ARSV) *Laurence M. Gould* (*LMG*), which frequently traverses Drake Passage, crossing the three main fronts of the ACC—Subantarctic Front, Polar Front, and Southern ACC Front; Fig. 1—to supply Palmer Station and conduct scientific cruises. The 153.6-kHz ADCP transducer is mounted in a sonar pod in the hull of the ship. The transducer depth is 6 m, the "blank-before-transmit" is 8 m, and the vertical depth bin is 8 m. A pulse length of 16 (8) m was used prior (post) November 2004, with the shallowest depth bin centered at 26 (22) m. Every other depth bin is approximately independent. Sonar pings are averaged in 300-s ensembles. An Ashtech GPS attitude sensing array (King and Cooper 1993) is used to correct gyrocompass heading, and the ship-relative currents are referenced to earth using P-code GPS. CODAS3 software (available online at http://currents.soest.hawaii.edu/software/codas3) is used to process and edit the data. Measurement errors in the absolute velocities computed from 300-s ensemble averages are of $O(1 \text{ cm s}^{-1}$; Chereskin and Harding 1993; Chereskin and Harris 1997) and are considerably less than the standard deviation of currents in Drake Passage $O(30–60 \text{ cm s}^{-1})$ over the record length of the observations in any given location.

This analysis incorporates ADCP data from 156 crossings between South America and the Antarctic Peninsula undertaken between September 1999 and October 2006. *LMG* cruise tracks in Drake Passage during this period are shown in Fig. 1. The Drake Passage high-resolution ADCP observations constitute an irregular time series of two-dimensional currents in the top 300 m in Drake Passage and are described by Lenn et al. (2007).

b. XBT–XCTD observations

Repeat expendable bathythermograph (XBT) and expendable conductivity–temperature–depth (XCTD)

surveys of Drake Passage, 6 times yearly, are also part of the ongoing observations conducted by the *LMG* and are described in detail by Sprintall (2003). XBT probes are deployed every 10–15 km between the 200-m isobaths at either end of Drake Passage, with higher resolution (5–10 km) across the Subantarctic Front and Polar Front (Fig. 1). XCTD probes were used intermittently on the early XBT surveys, and more recent XBT surveys include six XCTD probes evenly spaced across Drake Passage. Water temperatures and conductivity are consistently returned down to a depth of 800 m; depths determined from the fall rate model were expected to have a 3% accuracy below the mixed layer and better accuracy above (Wijffels et al. 2008). This study uses 37 XBT–XCTD surveys of upper-ocean temperature coincident with ADCP velocities between September 1999 and December 2004.

c. Winds

Four different gridded wind products covering the period September 1999 to October 2006 are used in this study. In each case, we have used the wind stress where provided or computed the wind stress from winds or psuedostresses at 10 m above sea level using drag coefficients from Yelland and Taylor (1996) for wind speeds in the 3–26 m s^{-1} range. For wind speeds outside of this range, we have assumed constant drag coefficients set to the minimum or maximum values determined from Yelland and Taylor (1996), as in Gille (2005). To match the region densely covered by ADCP observations, we have included only wind data points within the dashed line in Fig. 1.

The National Centers for Environmental Prediction–National Center for Atmospheric Research (NCEP–NCAR) global reanalysis project (Kalnay et al. 1996; Kistler et al. 1999) assimilates atmospheric data to estimate over 80 different variables on 28 vertical sigma levels. We computed wind stresses for this study from the NCEP–NCAR reanalysis 10-m winds, provided on a 192×94 Gaussian grid at 6-hourly intervals.

A second gridded wind product (IFR/CER) is produced by the Institut Francais de Recherche pour l'Exploitation de la Mer (IFREMER), Department of Oceanography and the Centre ERS d' Archivage et de Traitement (CERSAT). Daily mean winds at 10 m above sea level and surface wind stresses are estimated following a statistical interpolation of QuikSCAT scatterometer observations, using an objective method, onto a $0.5° \times 0.5°$ latitude–longitude grid. The IFREMER–CERSAT algorithm uses drag coefficients from Smith (1998) in the estimation of the IFR-/CER wind stresses included in this study. These data were obtained from CERSAT, at IFREMER, Plouzané, France.

A third wind product blends observations from the QuikSCAT scatterometer with the NCEP reanalysis (Milliff et al. 2004). To produce the high temporal and spatial resolution dataset (6-hourly, $0.5° \times 0.5°$ latitude–longitude grid), QuikSCAT swath wind retrievals are retained and augmented where absent with low-wave-number NCEP–NCAR reanalysis fields combined with a high-wavenumber component derived from QuikSCAT monthly statistics (algorithm adapted from Chin et al. 1998). Wind stresses used in this study are computed from the 10-m blended wind fields.

The Florida State University's Center for Ocean–Atmospheric Prediction Studies (COAPS) produces the fourth gridded wind product we considered. The COAPS wind product utilizes global data from the National Aeronautics and Space Administration (NASA) scatterometers (NSCAT and QSCAT) to map pseudo-stress wind values at $6 \text{ h} \times 1°$ latitude $\times 1°$ longitude resolution. The wind psuedostresses are produced by minimizing a cost function that matches the gridded values to the scatterometer data, and the wind divergence and curl to that of the background field (Pegion et al. 2000).

4. The wind-driven Ekman spiral

Wind-driven Ekman currents have been difficult to observe directly because, even when forced by strong winds, their magnitudes are small compared to the background geostrophic circulation. To recover the Ekman current signal from a total velocity measurement, the underlying geostrophic velocity must be subtracted from the observations. In the case of surface drifters, the local surface geostrophic current is inferred from instantaneous sea surface height and the remaining ageostrophic drifter velocity is attributed to Ekman currents (Rio and Hernandez 2003; Elipot 2006). If CTD observations are available together with shipboard ADCP measurements, the geostrophic shear may be estimated directly and subtracted from ADCP currents (e.g., Chereskin and Roemmich 1991). For other shipboard and moored ADCP current measurements, the geostrophic current is typically assumed to vary with depth much more slowly than the Ekman currents, and therefore may be represented by the total observed current at some level deep enough to be below the Ekman layer. The Ekman currents are then taken to be the currents remaining after this deep reference current has been subtracted from the observed currents at shallower depths (Price et al. 1987; Wijffels et al. 1994; Chereskin 1995). The challenge is to determine the depth at which the current is purely geostrophic, in other words, the depth of the Ekman layer.

It is reasonable to assume that the Ekman currents will be more steeply sheared with depth than the geostrophic currents, since they are driven by wind momentum input at the surface as opposed to large-scale density gradients. Consequently, we would expect the ageostrophic shear in the Ekman layer to exceed the geostrophic shear. The magnitude of the cross-track component of the geostrophic or baroclinic shear may be inferred from the XBT and XCTD observations in Drake Passage and is found to be approximately 10^{-4} s^{-1} in the top 300 m (Fig. 2a). This compares fairly well with the magnitude of the mean cross-track component of the shear in the ADCP currents, observed concurrently with the XBT–XCTD surveys, of about $1 \times 10^{-4} \text{ s}^{-1}$ below 100-m depth (Fig. 2b). Above 100 m, the mean ADCP shear deviates markedly from the geostrophic shear (Fig. 2b), indicating the presence of ageostrophic wind-driven Ekman currents. This implies that the base of the mean Ekman layer in Drake Passage is at or near 100-m depth.

Vertical profiles of the instantaneous ADCP currents referenced to 100-m depth were highly variable with time and location and also in terms of the rotation and the rate of amplitude decay with depth (not shown). This was most likely due to the high temporal variability in the winds, where frequent storms result in 4-day decorrelation time scales calculated for each of the wind products described in section 3c. Therefore, it was necessary to average the instantaneous ADCP currents referenced to 100-m depth to resolve a mean Ekman spiral in Drake Passage.

The ADCP currents are first sorted into $25 \text{ km} \times 25$ km grid boxes and averaged by transect to produce one velocity profile per transect per grid box for the region delineated in Fig. 1. The mean Ekman spiral ($\mathbf{U}_E$) was then extracted from the ADCP currents ($\mathbf{U}_A$) by subtracting the ADCP velocity at 98-m depth from ADCP velocities above 98 m in each gridded profile [$\mathbf{U}_E(z > -98) = \mathbf{U}_A(z > -98) - \mathbf{U}_A(z = -98)$] and averaging the gridded relative velocity profiles by grid box and then over all Drake Passage (Fig. 3); mean profiles from 332 grid boxes that are crossed at least twice by the *LMG* are included in the calculation. To estimate the degrees of freedom (DOF), we assumed that each crossing was independent, since crossings are at least four days apart. A meridional decorrelation length scale of 500 km in the wind field implies that there is one zonal and two meridional spatial DOF (Fig. 1) and thus 312 DOF for the standard error of the mean observed currents. This degree of averaging was required to resolve a reasonable mean Ekman current spiral (Fig. 3). Averaging subsets of ADCP velocity profiles sorted either by latitude or season resulted in transport
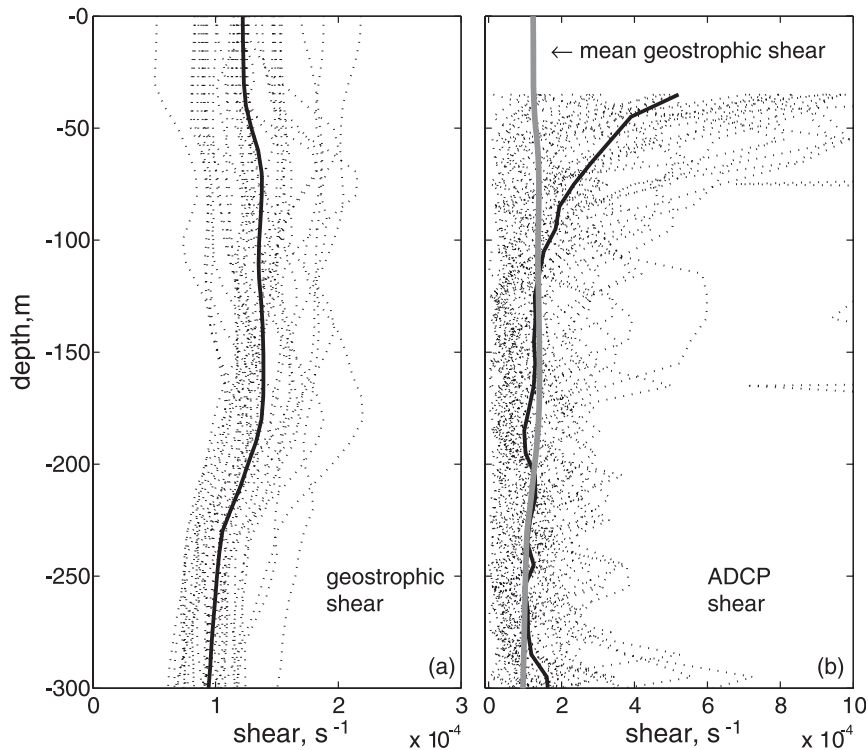
FIG. 2. Comparison of the magnitude of the cross-track component of (a) 5-yr mean geo-strophic shear (thick solid line) and section-averaged shear in the geostrophic velocities (dotted lines) relative to 800 m inferred from the Drake Passage XBT/XCTD surveys; (b) 5-yr mean ADCP shear (thick solid line), section-averaged ADCP shear (dotted lines) from the XBT surveys and the 5-yr mean geostrophic shear (thick gray line).

estimates that did not balance the mean surface wind stresses, although these current spirals were still useful for testing the reference depth choice.

The observed Drake Passage Ekman currents decay in amplitude with depth and spiral anticyclonically at depths below 26 m (Figs. 3 and 4a). Ageostrophic currents calculated using reference depths of 90 and 116 m (not shown) either did not resolve the full vertical structure of the Ekman currents or resulted in a reversal in the direction of rotation of the currents at the deepest level. To test the variation of the optimum reference depth with latitude, mean ageostrophic currents calculated from ADCP profiles sorted by latitude were used to locate the current spiral depths. The optimum reference depth appears to be independent of latitude and a constant 98 m across the Drake Passage region, located just above the base of the annual mean mixed layer at 120 m (Lenn et al. 2007; Sprintall 2003). In this regard, the Drake Passage Ekman layer depth differs from other directly observed Ekman layer depths at low-to-midlatitudes where Ekman spirals were observed to penetrate well below the mixed layer (e.g., Price et al. 1987; Chereskin and Roemmich 1991; Wijffels et al.
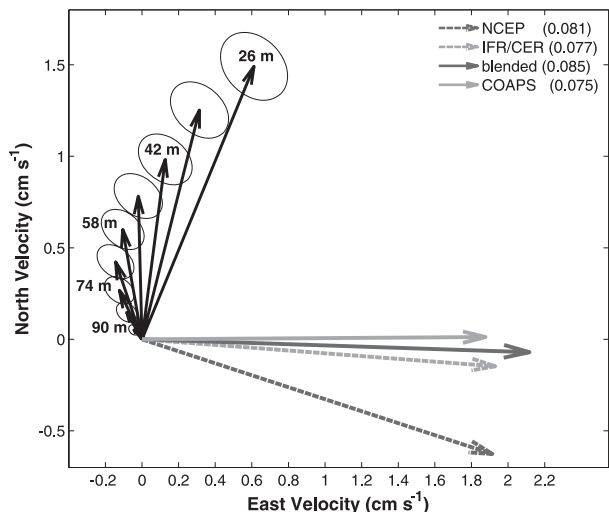

FIG. 3. Quiver plot of observed mean Ekman currents calculated from mean ADCP velocities relative to 98 m. Alternate depths of the Ekman currents are marked and the NCEP (dashed dark gray line), IFR/CER (dashed light gray line), blended (solid dark gray line), and COAPS (solid light gray line) mean wind stresses are shown; the magnitudes of the wind stresses are listed in units of N m^{-2} in parenthesis in the legend. Standard error ellipses are plotted at the tip of each current vector.
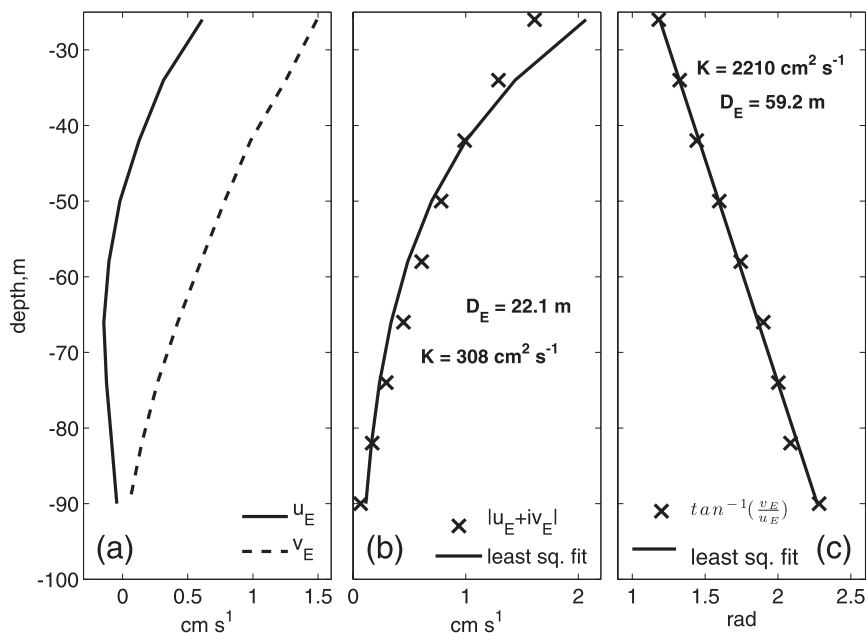
FIG. 4. Profiles of (a) observed mean Ekman currents in the zonal (solid line) and meridional (dashed line) directions; (b) amplitude of observed mean currents (crosses) and a least squares fit of exponentially decaying amplitude (solid line); and (c) rotation of Ekman velocity vector from the along-passage axis (crosses) and least squares fit of constant rotation rate with depth (solid line). The Ekman decay scales D_E and the eddy viscosities K inferred from the (b) least square fits of the exponentially decaying Ekman current amplitudes and (c) constant rotation rate with depth are also shown.

1994; Chereskin 1995). We were unable to get a statistically significant result, however, of the transport per unit mixed layer depth, as in Chereskin and Roemmich (1991), because of insufficient numbers of cruises with XBT data.

An exponential decay may be fitted by the least squares method to the observed decay in Ekman current amplitude (Fig. 4b). Applying the Ekman solutions [Eqs. (3) and (4)] to the least squares fit gives a decay scale of $D_E = 22.1$ m and an eddy viscosity of $K = 308$ cm^2 s^{-1}. A different and larger Ekman decay scale of $D_E = 59.2$ m and eddy viscosity $K = 2210$ cm^2 s^{-1} are predicted from the least squares fit of a constant rate of rotation with depth to the spiraling of the Ekman velocity vector (Fig. 4c). The observed time-averaged Ekman spiral is compressed such that the speed decays more rapidly than the current vector rotates with depth.

This order of magnitude discrepancy between the amplitude decay and the rotation rate of mean Ekman currents has also been noted on the few occasions where the Ekman balance has been observed in the open ocean, mostly at Northern Hemisphere midlatitudes (Price et al. 1987; Chereskin and Roemmich 1991; Wijffels et al. 1994; Chereskin 1995; Price and Sundermeyer 1999, hereafter PS99). In fact, Chereskin (1995) found quite similar values of the D_E (25 and 48 m) and K (274.2 and 1011 cm^2 s^{-1})

in the California Current, although the Ekman depth there is 48 m, which is deeper than the local mixed layer depth but about half the Ekman depth in Drake Passage. This observed compression of the time-averaged Ekman spiral points to weaknesses in Ekman theory [Eqs. (1)–(3)] that are discussed further in the section on turbulent stress (section 7).

5. Ekman transport

To compute Ekman transport from the observed mean Ekman currents, the observed Ekman spiral is integrated vertically upward from the base of the Ekman layer to the surface [Eq. (1)]. This calculation requires an extrapolation of the observations at 26-m depth to the surface. We chose to assume that the upper 26-m layer moves as a slab with the observed mean 26-m Ekman velocity, as previous observations of Ekman currents have provided evidence for the existence of a slab layer just below the surface (Price et al. 1986; Chereskin and Roemmich 1991; Wijffels et al. 1994). Careful consideration was also given to the calculation of errors that stem from the standard deviation of the observations and from the choice of reference depth (98 m). Calculating observed transport with reference depths of 90 and 116 m provides limits ($\pm r_z$) on the error as a result of

the reference depth choice, and this may be combined with the standard error ($\pm r_\sigma = \pm\sigma/\sqrt{312}$, where σ is the standard deviation of the gridded mean velocity profiles). The choice of reference depth and the standard errors in the observations each contribute about 50% to the total error. The observed Ekman transport (M_x, $M_y = 0.18 \pm 0.23$, 0.81 ± 0.19 m^2 s^{-1}) is predominantly equatorward with a 95% confidence ($\pm 2\sqrt{r_z^2 + r_\sigma^2}$) error ellipse that corresponds to a ~30% magnitude error and a ~19° directional error (Fig. 5). More observations would reduce the size of the error ellipse and improve the robustness of the observed transport estimate.

For comparison, we calculated the transports predicted from the wind products [Eq. (1)] and their associated 95% confidence error ellipses assuming 1 temporal degree of freedom every four days, and 1 zonal and 2 meridional degrees of freedom (Fig. 5). Although there is some agreement between the transports predicted from pairs of wind products, for example, IFR/CER and COAPS and blended and IFR/CER, the predicted Ekman transports do not converge on a single predicted transport; as they do not all agree at the 95% level (Fig. 5). The relative outlier in the predicted transports is inferred from the NCEP wind product; while the other three predicted Ekman transport are closer together (Fig. 5).

The observed transport is larger than the wind-predicted transports. Although the observed mean value falls outside all of the error ellipses for the wind-predicted transport, there is substantial overlap between error ellipses for the observations and the NCEP (most similar in magnitude) and blended (most similar in direction) Ekman transports; thus, the Ekman balance for these two wind products and the observations agree with 95% confidence. There is a moderate overlap between the confidence limits of the IFR/CER Ekman transport with that of the observed transport. The COAPS Ekman transport estimate, however, falls totally outside of the observed one; therefore, there is a less than 5% chance that these agree, assuming the error estimates are realistic.

The smaller error ellipses for the wind-predicted transports are much smaller than the error ellipse estimated for the observed transport (Fig. 5) because of the greater DOF ($\gg$312) in the gridded wind data. However, there are other uncertainties in the wind estimates that are difficult to assess but which would undoubtedly increase the estimated error. First, the scatterometer may underestimate wind speed and variance, since the instrument has not been extensively validated at high wind speeds. Moreover, the radar backscatter detected by the scatterometer intrinsically measures wind stress, but the quantity is calibrated to represent wind speed
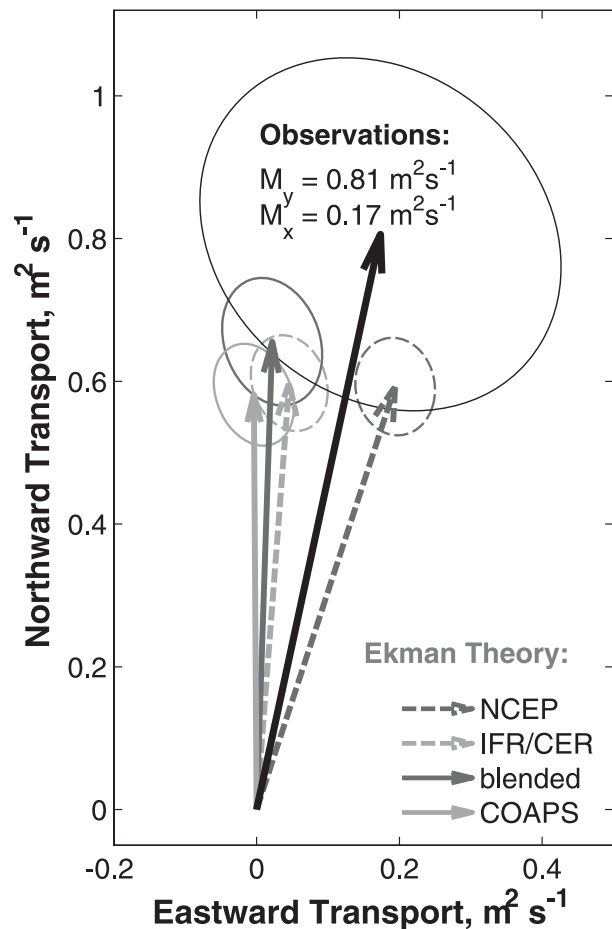

FIG. 5. Mean Ekman transport computed by integrating the observed mean Ekman currents, assuming the surface to 26-m currents move with the 26-m Ekman velocity (black arrow), and from the Ekman balance [Eq. (1)] predicted from the NCEP (dashed dark gray line), IFR/CER (dashed light gray line), blended (solid dark gray line), and COAPS (solid light gray line) mean wind stress in Drake Passage. The 95% confidence error ellipses are plotted.

and then converted to wind stress using drag coefficients that are not well validated for high wind speed conditions. The spatiotemporal interpolation and smoothing required to produce the gridded winds also likely result in a loss of resolution of the highest wavenumbers and frequencies and hence exclude extreme events that may produce higher mean stress estimates and variances.

6. Ekman layer temperature

Equatorward heat transport in the Ekman layer is a key component of the meridional overturning circulation of the Southern Ocean and acts in opposition to a poleward heat transport effected by transient eddies (de Szoeke and Levine 1981; Bryden 1979; Bryden and Heath 1985). The Ekman temperature flux

$\overline{\mathbf{U}_E T} = \bar{\mathbf{U}}_E \bar{T} + \overline{\mathbf{U}'_E T'}$ cannot be calculated directly with confidence as a function of latitude in Drake Passage due to the sparseness of the XBT data. A calculation based on profiles of temperature and velocity in one of the most densely sampled grid boxes in northern Drake Passage showed that $\overline{\mathbf{U}'_E T'}$ comprises only 1% of the local $\overline{\mathbf{U}_E T}$. The contribution from $\overline{\mathbf{U}'_E T'}$ is expected to be higher in southern Drake Passage, however, since T' is expected to be large compared to near-zero mean temperatures, but it cannot be determined with confidence given the fewer observations per grid box. Because the winds are latitudinally divergent over the Southern Ocean (Gille 2005), the mean observed Ekman spiral may also not be representative of the vertical structure of Ekman currents at every location in Drake Passage. We assume, therefore, that the slab-extrapolated observed mean Ekman spiral is representative of a location in the middle of Drake Passage, and that the error introduced by neglecting $\overline{\mathbf{U}'_E T'}$ and basing estimates of transport-weighted Ekman temperature on $\bar{\mathbf{U}}_E \bar{T}$ alone are likely to be no more than a few percent. The mean observed Ekman spiral and mean temperature $\bar{T}$, which we know with confidence, may then be used to directly estimate $\overline{\mathbf{U}_E T}$.

At 58°39.35″S 63°45.5l″W, in the middle of the Polar Front in Drake Passage, the transport-weighted Ekman temperature is 2.34 ±0.51°C and the surface (10 m) temperature at this location is 2.42°C. This implies that the mean surface temperature is a good proxy for the mean Ekman temperature, a result that will be useful for computing the Ekman layer heat flux when a reference temperature for the meridional heat flux is known. Mean surface temperatures increase equatorward across Drake Passage, and this is consistent with a buoyancy gain in the Ekman layer as it flows equatorward across the Polar Front as deduced by Speer et al. (2000).

7. Turbulent stress and Ekman layer eddy viscosities

Our attempt to estimate eddy viscosity K from the observed Ekman spiral (section 4) points to a fundamental problem with the theory: the assumption that the turbulent stress may be parameterized as a constant K times the vertical shear of horizontal currents [Eq. (2)]. A number of alternative theoretical models have been proposed that attempt to better describe wind-driven current dynamics by choosing different boundary conditions and/or allowing the eddy viscosity to vary with depth (e.g., Thomas 1975; Madsen 1977; Price et al. 1986; Lewis and Belcher 2004). By looking at spectral transfer functions of Ekman currents observed by surface drifters at 15-m depth and surface winds, Elipot (2006) deduced that the observations were best matched

by models in which the Ekman layer is finite with velocities that vanish at its base. Elipot (2006) also found that the performance of these finite-layer Ekman models was improved when the eddy viscosity K was allowed to vary linearly with depth to parameterize the increase in wind-forced turbulent eddy length scales, and hence eddy viscosity (Prandtl 1952), with depth. If K is allowed to vary with depth, Eq. (2) may be rewritten as

$$if \quad \mathbf{U}_E = \frac{1}{\rho}\frac{\partial \boldsymbol{\tau}(z)}{\partial z} = \frac{\partial}{\partial z}K(z)\frac{\partial \mathbf{U}_E}{\partial z}. \quad (5)$$

Integrating with respect to z gives the following relationship between the turbulent stress and the shear

$$\frac{\boldsymbol{\tau}(z)}{\rho} = K(z)\frac{\partial \mathbf{U}_E}{\partial z}. \quad (6)$$

Deducing the vertical structure of the eddy viscosity $K(z)$ then becomes a matter of estimating the turbulent stress and shear in the Ekman currents.

The mean turbulent stress profile may be estimated by integrating the mean observed Ekman currents vertically upward from the reference depth (h_E), such that

$$i\rho f \int_{-h_E}^z \overline{\mathbf{U}_E(z)}\,dz = \overline{\boldsymbol{\tau}(z)}. \quad (7)$$

Applying the zero velocity bottom boundary condition ($\overline{\mathbf{U}_E(-h_E)} = 0$ cm s^{-1}) and assuming that the mean Ekman currents above 26 m move as a slab layer with the 26-m mean Ekman velocity, we find that the stress increases as the depth shallows and approaches the mean surface wind stress values from all four wind products in Drake Passage (Fig. 6). As for the Ekman transport calculation, 95% confidence limits are estimated by combining standard errors in the observations and variations in the reference depth choice. Similarly, 95% confidence limits in the mean surface wind stresses are calculated by doubling the standard deviations of the respective wind stresses over the 7-yr period and assuming that there is one temporal DOF every four days, and one zonal and two meridional DOF in Drake Passage. We find that both zonal and meridional components of the estimated surface stress and the mean gridded wind stresses appear to match at 95% confidence (Fig. 6a). This is consistent with the errors in our transport calculation if one were to project the widths and heights of the error ellipses onto the zonal and meridional axes. A comparison of the stress error ellipses (Fig. 6b) confirms that, as in the transport calculation, the integrated Ekman surface stresses disagree with the mean COAPS and IFR/CER stresses and agree
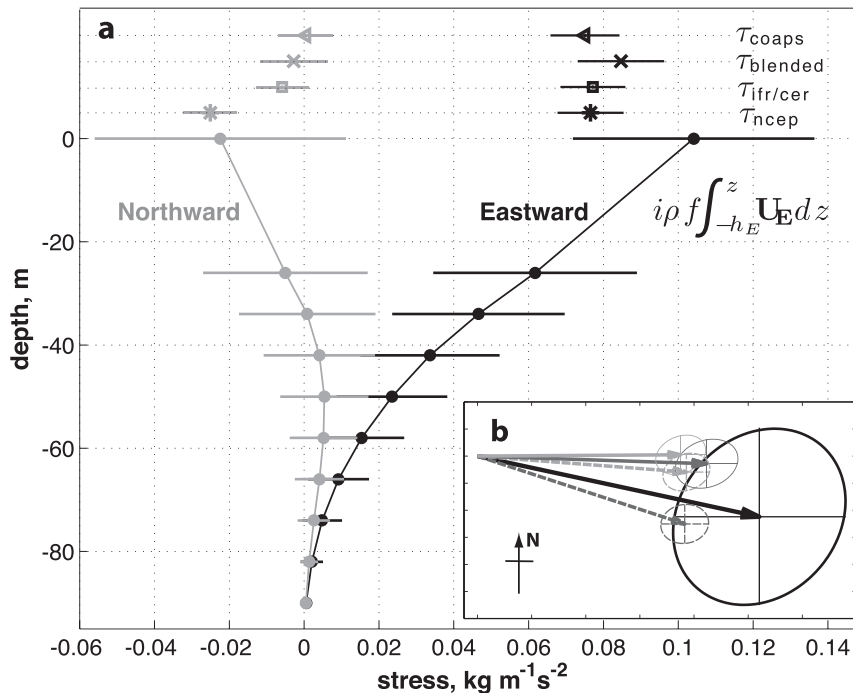
FIG. 6. (a) Eastward (black dots) and northward (gray dots) components of stress in the Ekman layer computed by integrating the Coriolis term vertically upward, assuming that velocity is zero at 98-m depth and a slab layer of the Ekman currents from 26-m depth to the surface. The mean eastward (black symbols) and northward components (gray symbols) of the NCEP (asterisks), IFR/CER (squares), blended (crosses), and COAPS (triangles) mean wind stress in Drake Passage are also shown; mean stresses from the different products are offset at 5-m intervals above 0-m depth for clarity. Error bars, corresponding to 95% confidence limits, for the turbulent stresses include both the standard deviation of the observations and possible errors due to the reference depth choice. (b) Scale drawing of the integrated stress (black) and mean NCEP (dashed dark gray line), IFR/CER (dashed light gray line), blended (solid dark gray line), and COAPS (solid light gray line) stresses, and associated 95% confidence error ellipses. Meridional and zonal 95% confidence intervals are plotted as crosshairs. Geographic north is shown in the bottom left corner.

with the mean blended and NCEP wind stresses at 95% confidence. This degree of agreement between the observations and gridded wind products provides confidence in our estimate of the turbulent stress profile.

The vertical shear calculated from the observed mean Ekman currents also decreases with depth (Fig. 7). The magnitude of the Ekman layer shear falls to 10^{-4} s^{-1} at 90-m depth (Fig. 7), corresponding to the mean XBT–XCTD geostrophic shear (Fig. 2). A second point of interest is that unlike the stress, the northward component of the shear is always positive in the Ekman layer, which means that the shear and stress vectors are not parallel. The stress vectors are found to be more nearly parallel to the wind stress than the shear vectors, particularly at the surface (Figs. 6 and 7). PS99 state that a nonparallel stress–shear relationship is consistent with a compressed Ekman spiral that results in the inference of a complex eddy viscosity $K(z)$ (Fig. 8) from Eq. (6).

The complex $K(z)$ inferred from the ratio of the observed stress (Fig. 6) and shear (Fig. 7) decreases in magnitude from ~1000 cm^2 s^{-1} at 26-m depth to near zero at the base of the Ekman layer (Fig. 8). The phase of $K(z)$ is always negative, indicating that the stress is rotated to the right of the corresponding shear vector, with the rotation increasing from 41.2° to 75.5° at deeper levels. These results are analogous to the findings of PS99 based on observations along a section at 10°N, where the inferred $|K(z)|$ also decreased from a value of ~600 cm^2 s^{-1} at about 20-m depth to near zero at 80-m depth. PS99 found the observed stress to be rotated to the left of the shear, increasing dramatically from −20° to ~45° over the 20–50-m depth range, below where the phase of $K(z)$ remains constant with depth. In an earlier analysis of moored surface observations in the California Current system by Chereskin (1995), the relative phase of stress and shear was neglected, and the eddy
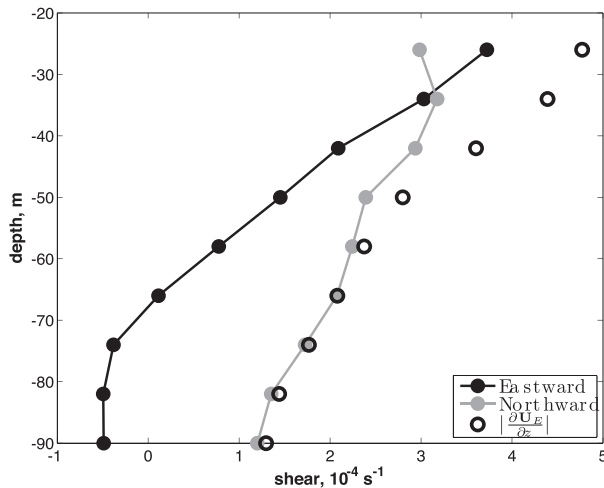
FIG. 7. Eastward (black dots) and northward (gray dots) components of shear in the Ekman layer computed from the observed mean Ekman currents. The magnitude of the shear is also shown (black circles).
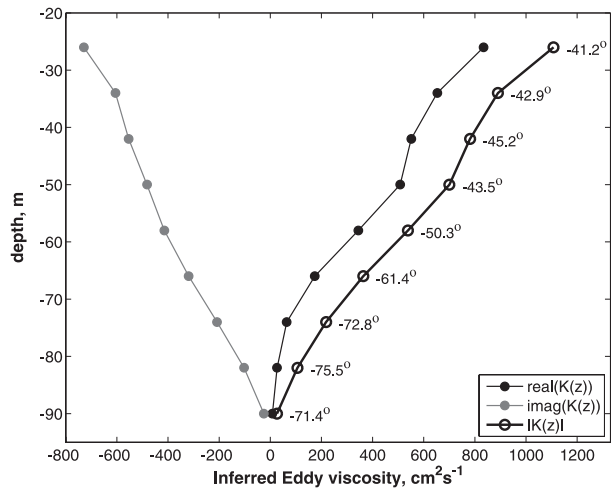

FIG. 8. Real (black dots) and imaginary (gray dots) components of the inferred eddy viscosity $K(z)$. The magnitude of the eddy viscosity $|K(z)|$ is also shown (black circles) together with the rotation angle of $K(z)$. Negative angles indicate that the stress is rotated to the right of the corresponding shear vector.

viscosity was inferred from the ratio of the magnitude of the stress to the magnitude of the shear. Chereskin (1995) found values of $|K(z)|$ in the 100–200 cm^2 s^{-1} range that decreased slightly with depth.

An interesting outcome of the Chereskin (1995) study was the examination of the production–dissipation balance hypothesis for the turbulent flux of momentum as a result of shear instabilities in the mean flow (e.g., Gregg et al. 1985; Dillon et al. 1989), in which

$$\frac{\boldsymbol{\tau}(z)}{\rho} = K(z)\frac{\partial \mathbf{U}_E}{\partial z} = \varepsilon \frac{\partial \mathbf{U}_E}{\partial z}\left|\frac{\partial \mathbf{U}_E}{\partial z}\right|^{-2}, \qquad (8)$$

where ε is the rate of dissipation that may be directly measured. Chereskin (1995) found that the total turbulent stresses inferred from the California Current velocity observations were in excellent agreement with a functional fit to Dillon et al.'s (1989) stress regression based on observed dissipation and shear in the equatorial Pacific. Similar wind conditions prevailed during both experiments. Chereskin's (1995) estimates of turbulent stress in the Ekman layer were of similar magnitude to our estimates in Drake Passage, and Chereskin's (1995) estimates also decreased in an approximately exponential fashion with depth. Chereskin (1995) concluded that within the Ekman layer, momentum is transferred by turbulence generated through shear instabilities.

PS99 opted for an alternative approach to understanding Ekman dynamics, choosing not to ignore the complex nature of $K(z)$ inferred from Eq. (6). Instead, PS99 considered several models of diffusion from which eddy diffusivity may be deduced, paying particular attention to the results of Price et al. (1986) and Wijffels et al. (1994), suggesting that a compressed Ekman spiral is produced by time-averaging well-mixed currents in a mixed layer that varies in depth in response to diurnal buoyancy fluxes. Using layered models that included the varying stratification, PS99 were able to make predictions of time-average Ekman current spirals that matched the observations. This led them to propose a complex laminar diffusion model with a complex turbulent eddy viscosity K that depends principally on the friction velocity ($U_* = \sqrt{\tau_o/\rho}$), maximum daily surface heat flux, the period of diurnal warming, and latitude. However, PS99 stressed that the complex K is formal and nonphysical, as the compression of the mean Ekman spiral is mainly an artifact of time averaging over the diurnal cycling in the stratification instead of physical properties of upper-ocean turbulence. Interestingly, a prediction by PS99 that at high latitudes the transport is trapped in the upper part of the Ekman layer, the "diurnal" layer, is consistent with our observations.

Another interpretation of the complex eddy viscosity is that it can be viewed as adding an asymmetric (or skewed) component in the stress tensor in Eq. (2) (P. Cessi 2008, personal communication). A nonparallel stress–shear relation could arise from the action of internal and surface gravity waves and their associated momentum flux. Surface gravity waves have already been shown to modify the surface boundary condition. Polton et al. (2005) showed that interaction between the surface wave–induced Stokes drift and the Coriolis force results in a vertical momentum transport that rotates

the time-averaged Ekman current spiral, such that the surface Ekman current is rotated to >45° from the mean wind stress (also seen in Fig. 3, assuming the surface moves with the 26-m velocity). This leads to questions of how the action of internal gravity waves may affect the subsurface structure of Ekman current spiral. Other physical processes that may affect the time-average Ekman currents include the mixed-layer response to high-frequency variability in the winds (McWilliams and Huckle 2006; Elipot 2006).

8. Conclusions

The Southern Ocean Ekman spiral extracted from the highly resolved but irregularly distributed Drake Passage ADCP observations provides the first observational evidence of the Ekman balance within the Antarctic Circumpolar Current. The observed time-mean Ekman currents decay in amplitude with depth and rotate anticyclonically from the surface. The observed mean Ekman transport appears to balance the momentum input by the surface wind stresses with 95% confidence (section 5), although the gridded wind products considered tended to underestimate the magnitude of the observed transport (Fig. 5). Surface temperature was at most 0.1°C higher than the transport-weighted temperature of the Ekman layer, and thus is a good approximation of the mean temperature transported equatorward by the Ekman flow.

As in other observations, the mean Ekman current spiral is compressed relative to predictions from Ekman theory that assumes a constant eddy viscosity K in the Ekman layer, decaying in amplitude more rapidly that it rotates with depth. By applying a modification to Ekman theory that assumes that turbulent stress within the wind-driven layer depends on a depth-dependent eddy viscosity $K(z)$ and the shear of the observed mean Ekman currents [Eq. (6)], we were able to infer $K(z)$ from the observations. The inferred $K(z)$ had magnitudes in the $O(10^2–10^3 \text{ cm}^2 \text{ s}^{-1})$ range and was complex, consistent with a compressed Ekman spiral where the stress is not parallel to the shear. Time-averaging observations subject to the diurnal cycling of the mixed layer (Price et al. 1986; Wijffels et al. 1994; PS99), the Coriolis–Stokes drift interaction due to surface wave actions (Polton et al. 2005), or nuances in the response of the wind-driven currents to high-frequency variability in the winds may all contribute to the observed compression of the Ekman spiral. Diurnal cycling of the mixed layer is not inconsistent with a turbulent transfer of momentum as a result of high shear instabilities (Chereskin 1995) expected at the base of the mixed layer. The challenge that remains is to quantify how these various mecha-

nisms may produce the apparent asymmetry in the shear–stress relation seen in open-ocean observations of Ekman currents.

REFERENCES

Bryden, H. L., 1979: Poleward heat flux and conversion of available potential energy in Drake Passage. *J. Mar. Res.,* **37,** 1–22.

——, and R. Heath, 1985: Energetic eddies at the northern edge of the Antarctic Circumpolar Current in the Southwest Pacific. *Prog. Oceanogr.,* **14,** 65–87.

Chereskin, T. K., 1995: Direct evidence for an Ekman Balance in the California Current. *J. Geophys. Res.,* **100,** 18 261–18 269.

——, and D. Roemmich, 1991: A comparison of measured and wind-derived Ekman transport at 11N in the Atlantic Ocean. *J. Phys. Oceanogr.,* **21,** 869–878.

——, and A. J. Harding, 1993: Modeling the performance of an acoustic Doppler current profiler. *J. Atmos. Oceanic Technol.,* **10,** 43–63.

——, and C. L. Harris, 1997: Shipboard acoustic Doppler current profiling during the WOCE Indian Ocean expedition: I10. Scripps Institution of Oceanography Tech. Rep. SIO 97–14, 137 pp.

——, and J. F. Price, 2001: Ekman transport and pumping. *Encyclopedia of Ocean Sciences,* J. Steele, S. Thorpe, and K. Turekian, Eds., Academic Press, 809–815.

Chin, T., R. Milliff, and W. Large, 1998: Basin-scale high-wave-number sea surface wind fields from multiresolution analysis of scatterometer data. *J. Atmos. Oceanic Technol.,* **15,** 741–763.

Deacon, G. E. R., 1937: *The Hydrology of the Southern Ocean.* Discovery Reports, Vol. 15, Macmillan, 1–124.

de Szoeke, R. A., and M. D. Levine, 1981: The advective flux of heat by mean geostrophic motions in the Southern Ocean. *Deep-Sea Res.,* **28A,** 1057–1085.

Dillon, T., J. Moum, T. Chereskin, and D. Caldwell, 1989: Zonal momentum balance at the equator. *J. Phys. Oceanogr.,* **19,** 561–570.

Ekman, V. W., 1905: On the influence of the earth's rotation on ocean-currents. *Ark. Mat. Astron. Fys.,* **2,** 1–52.

Elipot, S., 2006: Spectral characterization of Ekman velocities in the Southern Ocean based on surface drifter trajectories.

Ph.D. thesis, Scripps Institution of Oceanography, University of California, San Diego, 140 pp.

Gille, S. T., 2005: Statistical characterization of zonal and meridional wind stress. *J. Atmos. Oceanic Technol., 22,* 1353–1372.

Gregg, M., H. Peters, J. Wesson, N. Oakey, and T. Shay, 1985: Intensive measurements of turbulence and shear in the equatorial undercurrent. *Nature, 318,* 140–144.

Kalnay, E., and Coauthors, 1996: The NCEP/NCAR 40-Year Reanalysis Project. *Bull. Amer. Meteor. Soc., 77,* 437–471.

King, B. A., and E. B. Cooper, 1993: Comparison of ship's heading determined from an array of GPS antennas with heading from conventional gyrocompass measurements. *Deep-Sea Res. I, 40,* 2207–2216.

Kistler, R., and Coauthors, 1999: The NCEP–NCAR 50-Year Reanalysis: Monthly means CD-ROM and documentation. *Bull. Amer. Meteor. Soc., 82,* 247–267.

Lenn, Y.-D., T. K. Chereskin, J. Sprintall, and E. Firing, 2007: Mean jets, mesoscale variability and eddy momentum fluxes in the surface layer of the Antarctic Circumpolar Current in Drake Passage. *J. Mar. Res., 65,* 27–58.

Lewis, D., and S. Belcher, 2004: Time-dependent, coupled, Ekman boundary layer solutions incorporating Stokes drift. *Dyn. Atmos. Oceans, 37,* 313–351.

Madsen, O., 1977: A realistic model of the wind-induced Ekman boundary layer. *J. Phys. Oceanogr., 7,* 702–710.

McWilliams, J. C., and E. Huckle, 2006: Ekman layer rectification. *J. Phys. Oceanogr., 36,* 1646–1659.

Milliff, R., J. Morzel, D. Chelton, and M. Freilich, 2004: Wind stress curl and wind stress divergence biases from rain effects on QSCAT surface wind retrievals. *J. Atmos. Oceanic Technol., 21,* 1216–1231.

Orsi, A. H., T. Whitworth III, and W. D. Nowlin Jr., 1995: On the meridional extent and fronts of the Antarctic Circumpolar Current. *Deep-Sea Res. I, 42,* 641–673.

Pegion, P., M. Bourassa, D. Legler, and J. O'Brien, 2000: Objectively derived daily "wind" from satellite scatterometer data. *Mon. Wea. Rev., 128,* 3150–3168.

Polton, J. A., D. M. Lewis, and S. E. Belcher, 2005: The role of wave-induced Coriolis–Stokes forcing on the wind-driven mixed layer. *J. Phys. Oceanogr., 35,* 444–457.

Prandtl, L., 1952: *Essentials of Fluid Dynamics: With Applications to Hydraulics, Aeronautics, Meteorology and Other Subjects.* Blackie and Son, 452 pp.

Price, J. F., and M. A. Sundermeyer, 1999: Stratified Ekman layers. *J. Geophys. Res., 104* (C9), 20 467–20 494.

——, R. A. Weller, and R. Pinkel, 1986: Diurnal cycling: Observations and models of the upper ocean response to diurnal heating, cooling and wind mixing. *J. Geophys. Res., 91* (C7), 8411–8427.

——, ——, and R. R. Schudlich, 1987: Wind-driven ocean currents and Ekman transport. *Science, 238,* 1534–1538.

Rio, M.-H., and F. Hernandez, 2003: High-frequency response of wind-driven currents measured by drifting buoys and altimetry over the world ocean. *J. Geophys. Res., 108,* 3283, doi:10.1029/2002JC001655.

Sloyan, B. M., and S. R. Rintoul, 2001: The Southern Ocean Limb of the Global Deep Overturning Circulation. *J. Phys. Oceanogr., 31,* 143–173.

Smith, S. D., 1998: Coefficients for sea-surface wind stress, heat flux, and wind profiles as a function of wind speed and temperature. *J. Geophys. Res., 93* (C12), 15 467–15 472.

Speer, K., S. R. Rintoul, and B. Sloyan, 2000: The diabatic Deacon cell. *J. Phys. Oceanogr., 30,* 3212–3222.

Sprintall, J., 2003: Seasonal to interannual upper-ocean variability in the Drake Passage. *J. Mar. Res., 61,* 25–57.

Thomas, J. H., 1975: A theory of steady wind-driven currents in shallow water with variable eddy viscosity. *J. Phys. Oceanogr., 5,* 136–142.

Wijffels, S., E. Firing, and H. Bryden, 1994: Direct observations of the Ekman balance at 10°N in the Pacific. *J. Phys. Oceanogr., 24,* 1666–1679.

——, J. Willis, C. M. Domingues, P. Barker, N. J. White, A. Gronell, K. Ridgway, and J. A. Church, 2008: Changing expendable bathythermograph fall rates and their impact on estimates of thermosteric sea level rise. *J. Climate, 21,* 5657–5672.

Yelland, M., and P. K. Taylor, 1996: Wind stress measurements from the open ocean. *J. Phys. Oceanogr., 26,* 541–558.